Supplementary Material for "A Regularized Model-based Optimization Framework for Pan-Sharpening"

Hussein A. Aly and Gaurav Sharma

This document provides supplementary material, for the paper [1]. We provide spectral sensitivities of the IKONOS imaging channels (Section S.I), details of spatial filters $h_i[\mathbf{x}]$ used in our pan-sharpening formulation along with their frequency responses(Section S.II), maps showing the valid data regions for the IKONOS datasets from [2] used in our work (Section S.III), registration parameters for registering the spectral images in the different datasets to their panchromatic counterparts (Section S.IV), image results that are not included in the main paper due to page length constraints (Section S.V), and a discussion of the convergence behavior for the proposed pan-sharpening algorithm (Section S.VI).

S.I. Spectral Sensitivities $\tau_i(\lambda), i = 0, 1, \ldots 4$ for the IKONOS Satellite

Figure S.1 shows the spectral sensitivities for the IKONOS imager, normalized to a maximum value of 1, i.e., $\tau_i(\lambda)/\nu_i$ with $\nu_i = \max_\lambda \tau_i(\lambda)$ for $i = 0, 1, \ldots 4$, corresponding respectively to the panchromatic, B, G, R, and NIR, channels, respectively. Actual sensitivities, required for our subsequent computations are obtained by combining these with appropriate gain factors ν_i provided in [3].

S.II. Spatial Filters $h_i[\mathbf{x}], i = 0, 1, \ldots 4$

We model $\mathcal{H}_i^\Gamma(\chi, \upsilon)$ for $i = 0, 1, \ldots, 4$ as filters with a Gaussian frequency response having a value of unity at frequency $(0, 0)$ and a value at the Nyquist limit that is obtained from [3] and indicated in

H. A. Aly is with Military Technical college (MTC), Ministry of Defense, Cairo, Egypt. This work was partly conducted while he was visiting at the Department of Electrical and Computer Engineering, University of Rochester, Rochester, NY 14627-0126 USA. (E-mail: haly@ieee.org, hussein.aly@rochester.edu)

G. Sharma* is with the Department of Electrical and Computer Engineering, University of Rochester, Rochester, NY 14627-0126 USA. (E-mail: g.sharma@ieee.org)
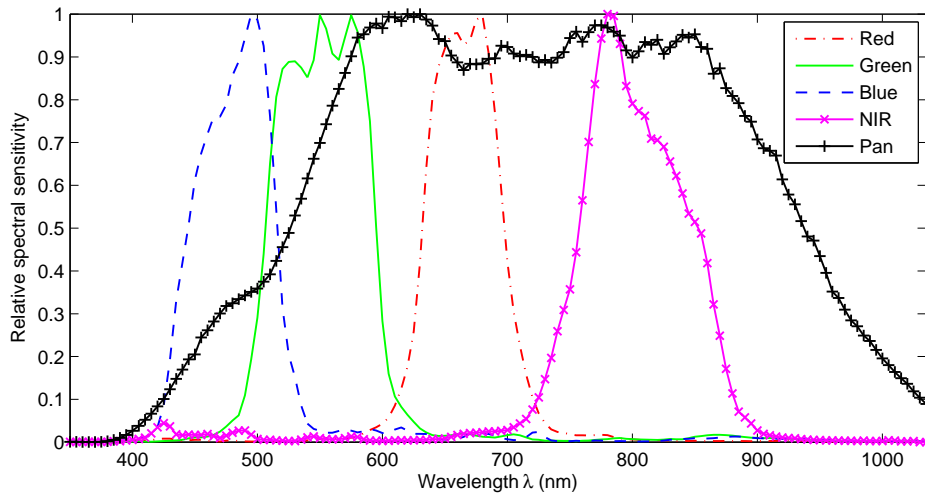
Fig. S.1. Relative spectral sensitivities of the panchromatic and the spectral imaging bands for the IKONOS multispectral imaging satellite [4]

Table S.I. The filters $h_i[\mathbf{x}], i = 0, 1, \ldots, 4$ are then designed using the method of [5] as zero-phase finite-impulse-response (FIR) filters with a square spatial support for the impulse response that is symmetric about the origin. Specifically, the filters $h_i[\mathbf{x}], i = 0, 1, 2, 3$ have a spatial support of 11×11 pixels and $h_4[\mathbf{x}]$ has a spatial support of 15×15 pixels. A parametric model is utilized for the image power spectral density required in the filter design process, which is also described in [5]. We note that the methodology of [5] is general and applicable to arbitrary choices of $\mathcal{H}_i^\Lambda(\chi, \upsilon)$ and $\mathcal{H}_i^\Gamma(\chi, \upsilon)$.

Figure S.2 shows the magnitude frequency responses $|H_i(u, v)|$ corresponding to the spatial filters $h_i[\mathbf{x}]$, for $i = 0, 1, \ldots 4$, i.e., the panchromatic, blue, green, red, and NIR channels, respectively. The filters for the different channels exhibit similar characteristics although differences in the specifications are indeed reflected in the designed filters as can be seen from the magnitude $|H_i(u, v)|$ of the frequency response at the cut-off frequency $\sqrt{u^2 + v^2} = \frac{1}{2qX}$ and the 3dB bandwidth listed in the third and fourth columns, respectively, of Table S.I. Because the panchromatic channel has a much sharper fall-off (a lower MTF at the Nyquist frequency) the corresponding spatial filter frequency response $|H_0(u, v)|$ demonstrates a more rapid fall-off than the spatial filters $h_i[\mathbf{x}], i = 1, 2, 3, 4$ for the spectral channels. Some side-lobes are also visible in the plot for $|H_0(u, v)|$, although they are not a concern because the side-lobe peaks are almost 30 dB below the main lobe peak.

i	Spectral Band	MTF at Nyquist	$\lvert H_i(u,v) \rvert$ at cut-off	3dB bandwidth for $H_i(u,v)$ (fraction of cut-off freq.)
0	**PAN**	0.170	0.1833	0.65
1	**BLUE**	0.266	0.2873	0.75
2	**GREEN**	0.284	0.3060	0.76
3	**RED**	0.290	0.3122	0.78
4	**NIR**	0.277	0.2987	0.76

TABLE S.I

SPATIAL FILTER SPECIFICATIONS FOR THE PANCHROMATIC AND THE SPECTRAL CHANNELS. THE THIRD COLUMN OF THE TABLE LISTS THE MTF FOR $\mathcal{H}_i^{\Gamma}(\chi, v)$ FOR $i = 0, 1, \ldots, 4$ AT THE NYQUIST LIMIT BASED ON [3]. THE THIRD COLUMN LISTS THE FREQUENCY RESPONSES FOR THE FILTERS $h_i[\mathbf{x}], i = 0, 1, \ldots, 4$ AT THE CUT-OFF FREQUENCY $\sqrt{u^2 + v^2} = \frac{1}{2qX}$ AND THE CORRESPONDING 3DB BANDWIDTH IS INDICATED IN THE FOURTH COLUMN AS A FRACTION OF THE CUT-OFF FREQUENCY.

S.III. DATA VALIDITY REGIONS

The IKONOS datasets obtained from [2] have valid image data over irregularly shaped regions that are shown in Fig. S.3 in relation to the rectangular tiles over which the image data is provided. The statistics reported in the manuscript are computed over these valid data regions.

S.IV. REGISTRATION PARAMETERS

The images we use in our experiments are registered at the resolutions at which they are provided. Pan-sharpening, however, generates higher resolution versions of these images where sub-pixel shifts between the individual spectral images and the panchromatic image can become significant. We therefore upsample each LR spectral image from Γ to Λ using constrained least squares and estimate the registration between the resulting image and the panchromatic image as the coordinate shift $(\Delta x, \Delta y)$ for the upsampled spectral image that maximizes the correlation with the HR panchromatic image, where this shift is determined by a search in a small two-dimensional neighborhood about $(0, 0)$. Table S.II lists the shift parameters $(\Delta x, \Delta y)$ for each of the spectral channels for each of the test images used in our experiments. These shifts are incorporated in all of the pan-sharpening methods.

S.V. ADDITIONAL IMAGE RESULTS

IMPORTANT: The images are best viewed in their native TIFF format versions submitted as supplementary material with the paper, where differences can be studied by examining under zoom with
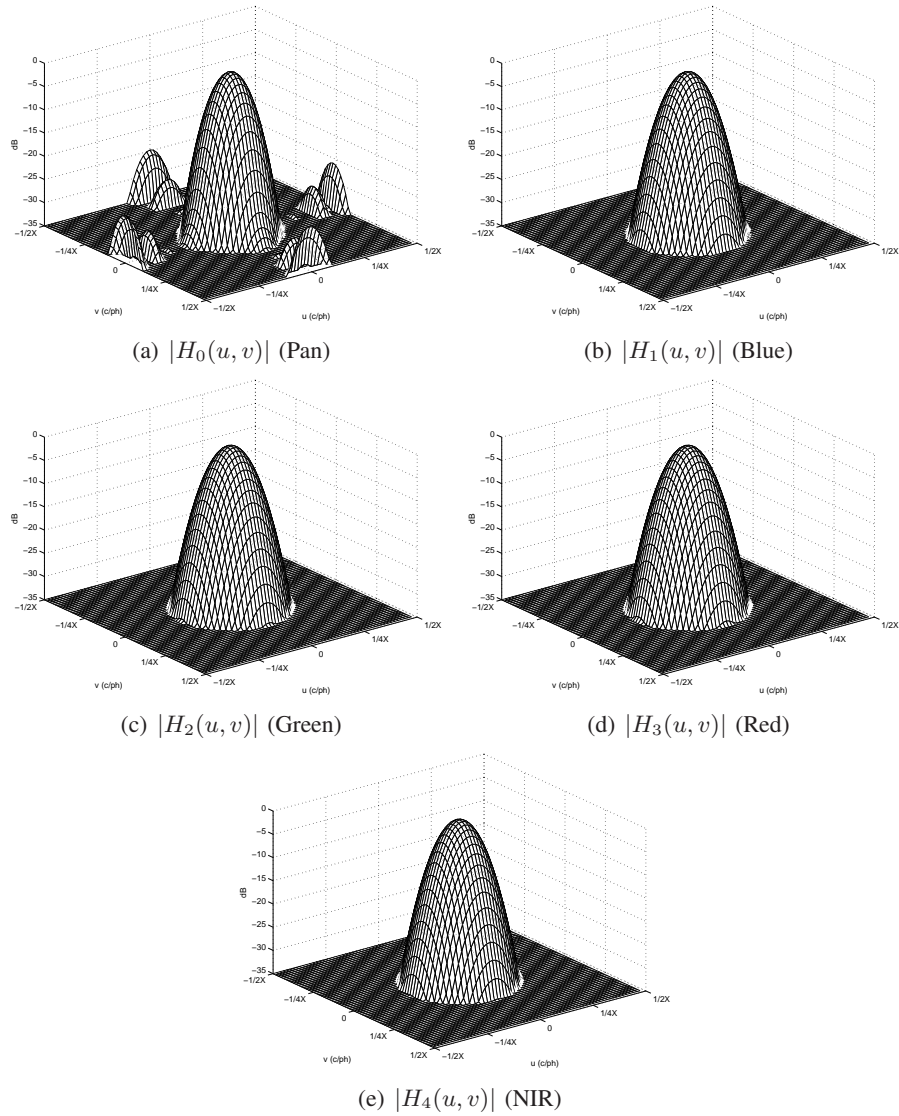
3

(a) $|H_0(u,v)|$ (Pan)

(b) $|H_1(u,v)|$ (Blue)

(c) $|H_2(u,v)|$ (Green)

(d) $|H_3(u,v)|$ (Red)

(e) $|H_4(u,v)|$ (NIR)

Fig. S.2. Frequency $|H_i(u,v)|$ responses corresponding to the spatial filters $h_i[\mathbf{x}]$ for $i = 0, 1, 2, \ldots 4$.

a suitable image viewer. Images in electronic PDF versions of the paper, may be subject to compression or post-processing in the publication process which may mask actual differences or introduce spurious variations. Each figures caption identifies the corresponding TIFF file.

Figure S.4 continues the presentation of Fig. 3 by showing pan-sharpened results for the R, G, B bands obtained with additional methods for the same dataset as in Fig. 3. Figures S.5 and S.6 present the pan-sharpened images for the NIR channel for the sample dataset whose R, G, B components were previously presented in Figs. 3 and S.4. The presentation format for the NIR images mirrors the one

(a) Image 58204   (b) Image 58205   (c) Image 58207   (d) Image 58208
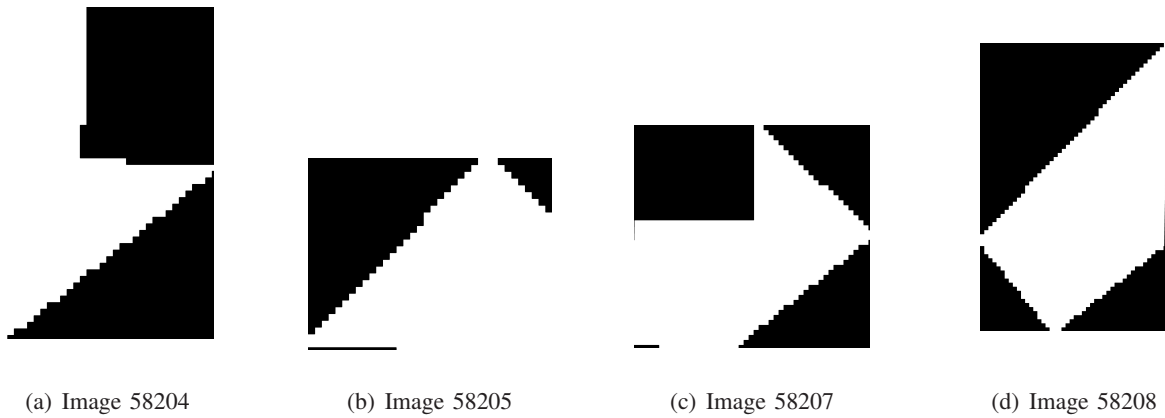
Fig. S.3. Maps of the data validity regions for the IKONOS datasets **China-Sichuan** $xxxxx\_0000000.2000xxxx$ from [2]

Image sample	Red		Green		Blue		NIR	
	Δx	Δy	Δx	Δy	Δx	Δy	Δx	Δy
58204_0000000.20001116	0	0	0	0	0	0	0	0
58205_0000000.20001003	2	1	2	1	1	2	3	1
58207_0000000.20000831	2	2	2	2	2	1	3	2
58208_0000000.20001108	2	1	3	1	2	1	3	1

TABLE S.II

ESTIMATED SHIFTS FOR REGISTERING UPSAMPLED VERSIONS OF THE LR SPECTRAL IMAGES TO THE CORRESPONDING HR PANCHROMATIC IMAGE FOR THE IKONOS IMAGE SETS FROM GEOEYE [2] USED IN OUR EXPERIMENTS.

used for the combined R, G, B image where the individual images in the collage are identified by labels (placed below). Please see text in the main manuscript for elaboration. The proposed method (Prop) provides pan-sharpened NIR images that are sharper than the images obtained the other methods, with the exception of the Gram-Schmidt (GS) technique, which offers sharper images. Upon viewing the images under reduction, we see that the image obtained by reducing the resolution of the image obtained with the proposed technique (Prop) has a better agreement with the observed dynamic range in the low-resolution image (Prop). This suggests that the (GS) technique appears to have over-sharpened the NIR channel image in a manner that is not completely consistent with the observed low resolution data for this channel.

Pan-sharpened image results for a small region from another dataset are presented in Figs. S.7–S.10 in an format to those for Figs. 3, S.4, S.5, and S.6. The results in Figs. S.7 and S.9 exhibit the same trends as seen in Figs. 3 and S.5 providing further support for our conclusions.

Supplementary data included with this paper provide additional images from the other datasets used in our evaluation (in TIFF format). These images allow visual comparison between the proposed methods.

GIHS

MSW3

Prop-PC

Prop-AP

Prop-NR

6

Prop-CLS

Fig. S.4. Sample pan-sharpening result for a potion of the **China-Sichuan** 58208_0000000.20001108 dataset for the R, G, B channels (See **FullResCompare2_58208_MS.tif**). Images are identified by the labels (placed below). See caption for Fig. 3 and text for additional details. The corresponding NIR channel results can be found in the supplementary materials (File **FullResCompare2_58208_NIR.tif**).

BC

PAN

Prop

GS

GIHSA

7

MBTV

Fig. S.5. Sample pan-sharpening result for a potion of the **China-Sichuan** 58208_0000000.20001108 dataset for the NIR channel (See **FullResCompare1_58208_NIR.tif**). Images are identified by the labels (placed below). See caption for Fig. 3 and text for additional details. The corresponding R, G, B channel results can be found in Fig 3 (File **FullResCompare1_58208_MS.tif**).
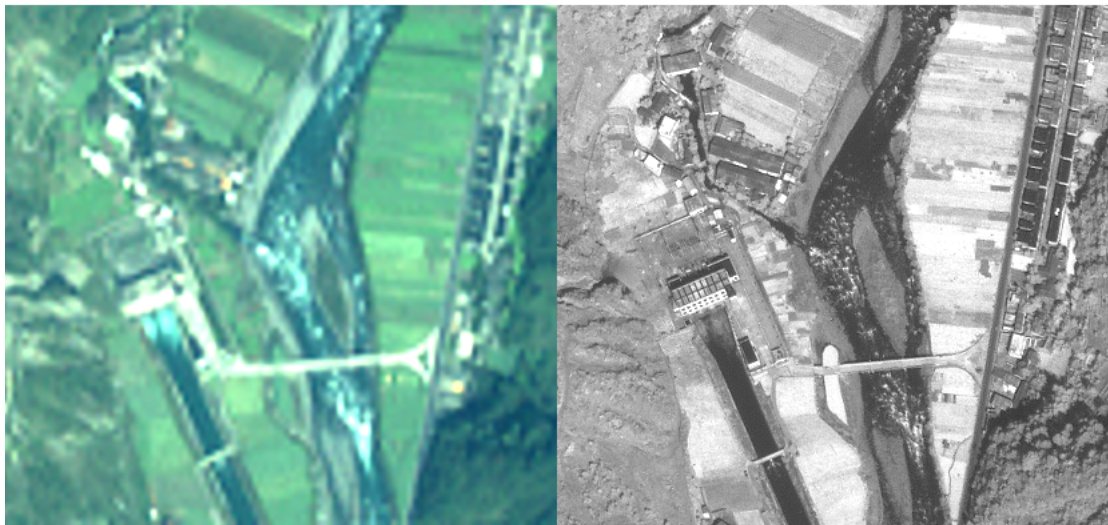
GIHS

MSW3

Prop-PC

Prop-AP

Prop-NR

8

Prop-CLS

Fig. S.6. Sample pan-sharpening result for a potion of the **China-Sichuan** 58208_0000000.20001108 dataset for the NIR channel (See **FullResCompare2_58208_NIR.tif**). Images are identified by the labels (placed below). See caption for Fig. 3 and text for additional details. The corresponding R, G, B channel results can be found in Fig S.4 (File **FullResCompare2_58208_MS.tif**).

BC

PAN

Prop

GS

GIHSA

9

MBTV

Fig. S.7. Sample pan-sharpening result for a potion of the **China-Sichuan** 58205_0000000.20001003 dataset for the MS channel (See **FullResCompare_58205_MS.tif**). Images are identified by the labels (placed below). See caption for Fig. 3 and text for additional details. The corresponding NIR channel results can be found in the Fig. S.9 (File **FullResCompare_58205_NIR.tif**).
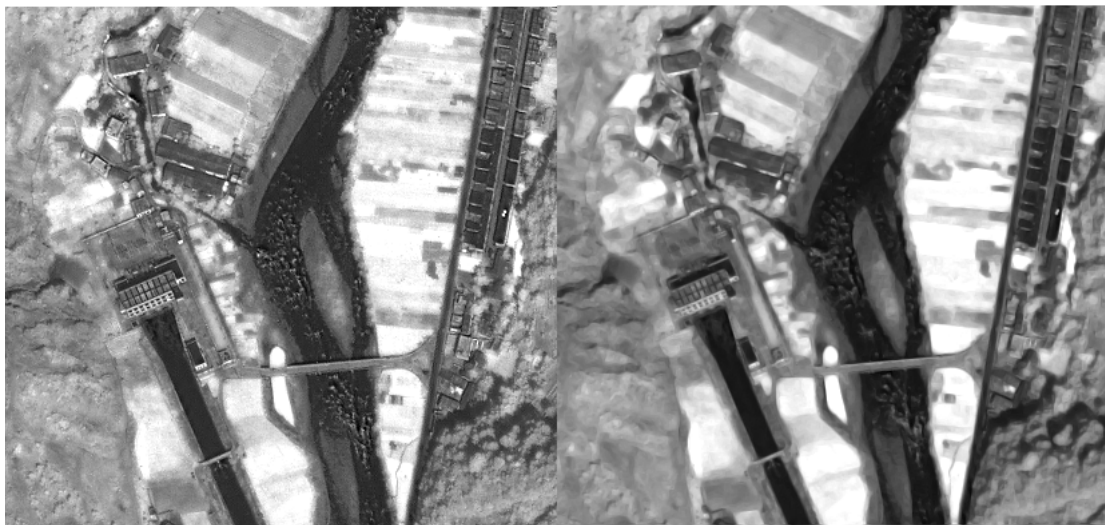
GIHS

MSW3

Prop-PC

Prop-AP

Prop-NR

Prop-CLS

Fig. S.8. Sample pan-sharpening result for a potion of the **China-Sichuan** 58205_0000000.20001003 dataset for the MS channel (See **FullResCompare2_58205_MS.tif**). Images are identified by the labels (placed below). See caption for Fig. 3 and text for additional details. The corresponding NIR channel results can be found in the Fig. S.9 (File **FullResCompare2_58205_NIR.tif**).
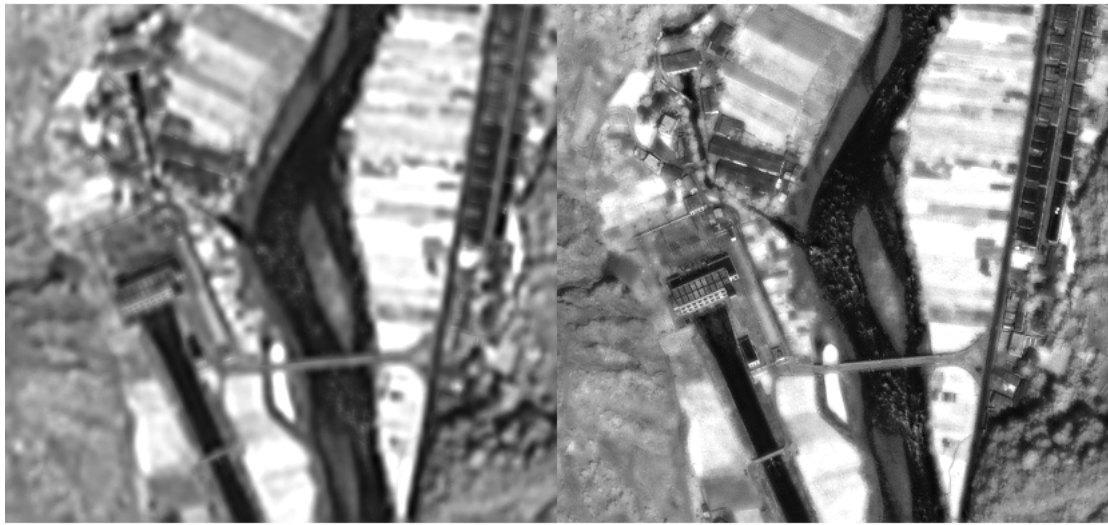
BC

PAN

Prop

GS

GIHSA

11

MBTV

Fig. S.9. Sample pan-sharpening result for a potion of the **China-Sichuan** 58205_0000000.20001003 dataset for the NIR channel (See **FullResCompare_58205_NIR.tif**). Images are identified by the labels (placed below). See caption for Fig. 3 and text for additional details. The corresponding R, G, B channel results can be found in Fig. S.7 (File **FullResCompare_58205_MS.tif**).
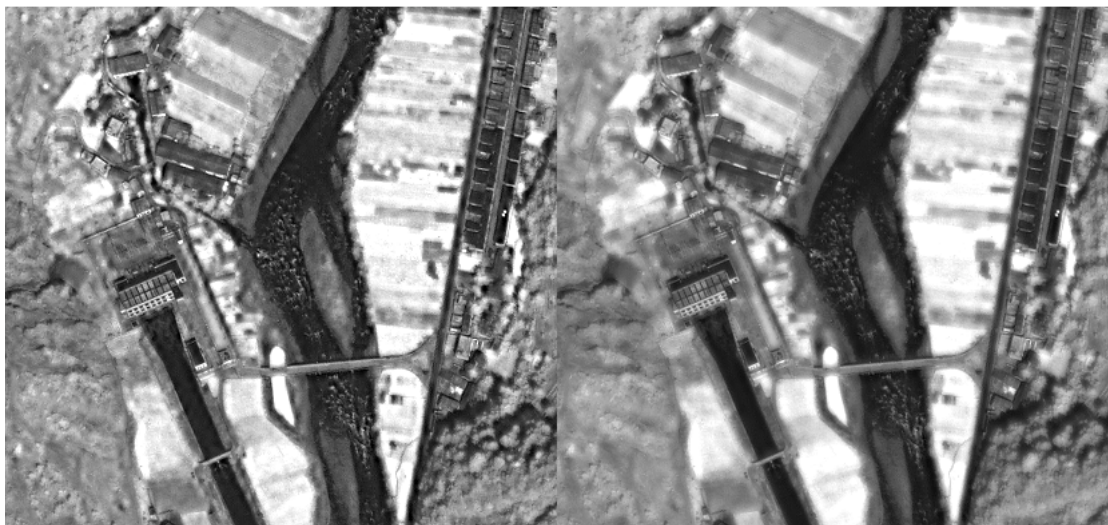
GIHS

MSW3

Prop-PC

Prop-AP

Prop-NR

12

Prop-CLS

Fig. S.10. Sample pan-sharpening result for a potion of the **China-Sichuan** 58205_0000000.20001003 dataset for the NIR channel (See **FullResCompare2_58205_NIR.tif**). Images are identified by the labels (placed below). See caption for Fig. 3 and text for additional details. The corresponding R, G, B channel results can be found in Fig. S.8 (File **FullResCompare2_58205_MS.tif**).

To facilitate easy comparison and assimilation of the results, the files provided adopt the same format and the same naming conventions as the images are presented in the paper. The results for these additional datasets exhibit trends to similar to those seen for the images presented in the paper. Please see the main manuscript for a description of these trends and for guidance in viewing the images that allows some of the differences to be clearly seen.

A. Images Obtained from Simulations

The results presented in Table I of the main manuscript were obtained through simulations. In this section, we also present a subset of the corresponding images to allow visual comparisons. Figures S.11 and S.12 show the results obtained under the simulation scenario for (approximately) the same region as was used in Figs. 3 and S.5, where the images are also presented in an identical manner for the R, G, B and NIR channels. The images compared in this case also include the original images (Orig) that are available for the simulation setting and results obtained with the GIHSA and MSW3 methods. Because the images for the simulation are reduced in resolution compared to their native captured versions, differences between these images (in Fig. S.11 and its TIFF counterpart) are hard to assess visually. For the simulations, consistent with the numerical metrics presented in the paper, the pan-sharpened NIR image obtained via the proposed method appears closer in appearance to the original NIR image compared with other methods. Other differences are hard to appreciate visually and we therefore refer to the numerical metrics already presented in the main manuscript for comparing the different methods in the simulations.

S.VI. CONVERGENCE BEHAVIOR

We examined the convergence of the proposed method by plotting the objective function in (8) as a function of the iteration count. A representative plot is shown in Fig S.13 for one of the datasets. The plot illustrates that the algorithm converges quite rapidly and between 15 to 20 iterations the objective function achieves a value close to its minimum (which motivated our gradient scaling schedule beyond iteration $N_0 = 20$). The plot also illustrates the monotone convergence expected from the convexity of the problem upto the small variations seen in general with gradient descent methods with a fixed step size. Because the different terms in the objective function may converge at different rates and in order to minimize the gradient noise in the final optimization, we conservatively set the number of iterations to a
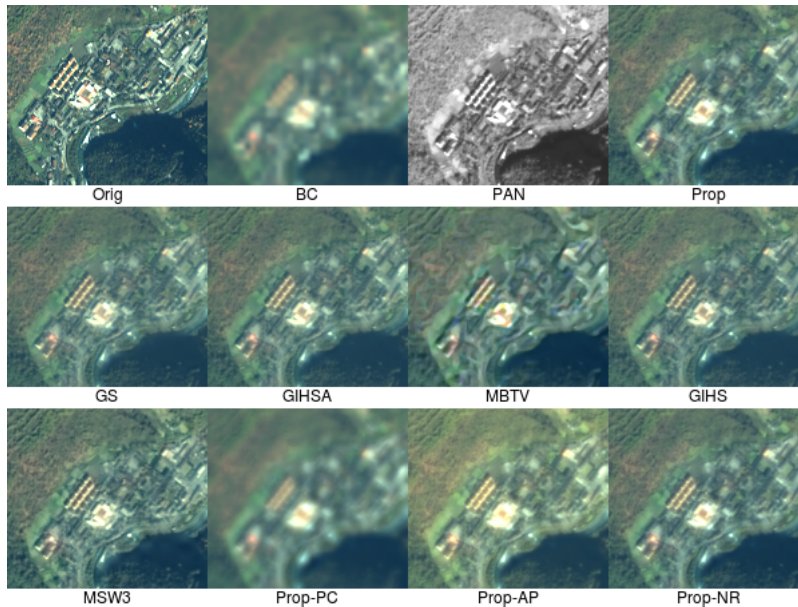
Fig. S.11. Sample result from simulations conducted with the **China-Sichuan** 58208_0000000.20001108 dataset (See **SimCompare_58208_MS.tif**). The R, G, and B spectral channels presented as a three channel image. Images are identified by the labels (placed below): Orig - the high-resolution ground-truth multispectral image; BC - the low-resolution multispectral image, interpolated via bicubic interpolation to match the original's size, (c) PAN - the high-resolution panchromatic image, that along with the low-resolution multispectral image forms the input to the pan-sharpening algorithm. The pan-sharpened images are labeled Prop, GS, GIHS, GIHSA, MSW3, MBTV in correspondence with their respective algorithms, i.e. the proposed method, Gram-Schmidt [6], generalized IHS [7], generalized IHS adaptive [8], multi-scale wavelet with 3 levels of decomposition [9], and the MBO total variation regularized approach of [10]. See text for additional details. The corresponding NIR channel results can be found in the supplementary materials Fig. S.12 (File **SimCompare_58208_NIR.tif**).

fixed count of $N_{\max} = 50$. While this makes the algorithm fairly demanding computationally, it assures that the results are close to the best possible results obtainable with the proposed method.

REFERENCES

[1] H. Aly and G. Sharma, "A regularized model-based optimization framework for pan-sharpening," *IEEE Trans. Image Proc.*, vol. 23, 2014, accepted for publication April 07, 2014, to appear, DOI: 10.1109/TIP.2014.2316641.

[2] Space-Imaging, "Geoeye IKONOS scene data," 2000. [Online]. Available: ftp://ftp.glcf.umiacs.umd.edu/glcf

[3] M. Cook, B. Peterson, G. Dial, L. Gibson, F. Gerlach, K. Hutchins, R. Kudola, and H. Bowen, "IKONOS technical performance assessment," in *Algorithms for Multispectral, Hyperspectral, and Ultraspectral Imagery VII*, S. S. Shen and M. R. Descour, Eds., vol. 4381, Aug. 2001, pp. 94–108.

[4] G. Dial, H. Bowen, F. Gerlach, J. Grodecki, and R. Oleszczuk, "IKONOS satellite, imagery, and products," *Remote sensing of Environment*, vol. 88, no. 1, pp. 23–36, 2003.

[5] H. A. Aly and E. Dubois, "Specification of the observation model for regularized image up-sampling," *IEEE Trans. Image Process.*, vol. 14, no. 5, pp. 567–576, May 2005.
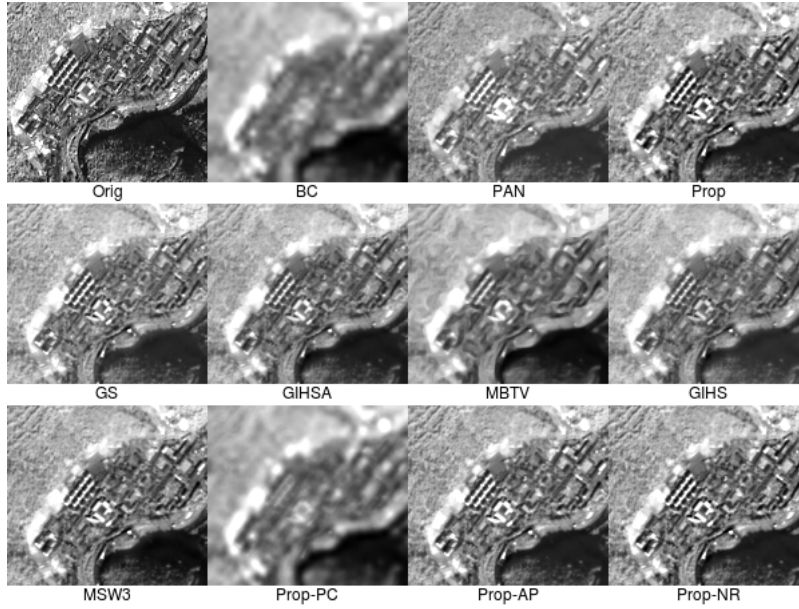
14

Fig. S.12. Sample result from simulations conducted with the **China-Sichuan** 58208_0000000.20001108 dataset (See **SimCompare_58208_NIR.tif**) for the NIR channel. Images are identified by the labels (placed below). See caption for Fig. S.11 and text for additional details. The corresponding R, G, B channel results can be found in Fig. S.11 (File **SimCompare_58208_MS.tif**).
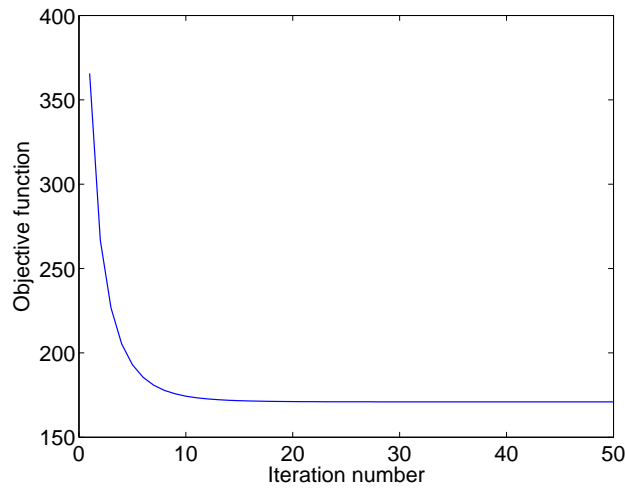

Fig. S.13. The objective function (8) as a function of the iteration count for the proposed algorithm on the sample **China-Sichuan** 58207_0000000.20000831 dataset.

[6] C. Laben and B. Brower, "Process for enhancing the spatial resolution of multispectral imagery using pan-sharpening," U.S. Patent 6011875, Eastman Kodak Company, Jan. 2000.

[7] T. Tu, S. Su, H. Shyu, and P. Huang, "A new look at IHS-like image fusion methods," *Elsevier: Inf. fusion*, vol. 2, pp. 177–186, 2001.

[8] B. Aiazzi, S. Baronti, and M. Selva, "Improving component substitution pansharpening through multivariate regression of MS+ Pan data," *IEEE Trans. Geosci. Remote Sens.*, vol. 45, no. 10, pp. 3230–3239, Oct. 2007.

[9] T. Ranchin and L. Wald, "Fusion of high spatial and spectral resolution images: the ARSIS concept and its implementation," *Photogram. Eng. Remote Sens.*, vol. 66, no. 1, pp. 49–61, 2000.

[10] F. Palsson, J. Sveinsson, and M. Ulfarsson, "A new pansharpening algorithm based on total variation," *IEEE Geosci. Remote Sens. Lett.*, vol. 11, no. 1, pp. 318–322, 2014.